Volume 12
Number 11
November 2025
Pages 4739–5090

Environmental Science Nano

rsc.li/es-nano

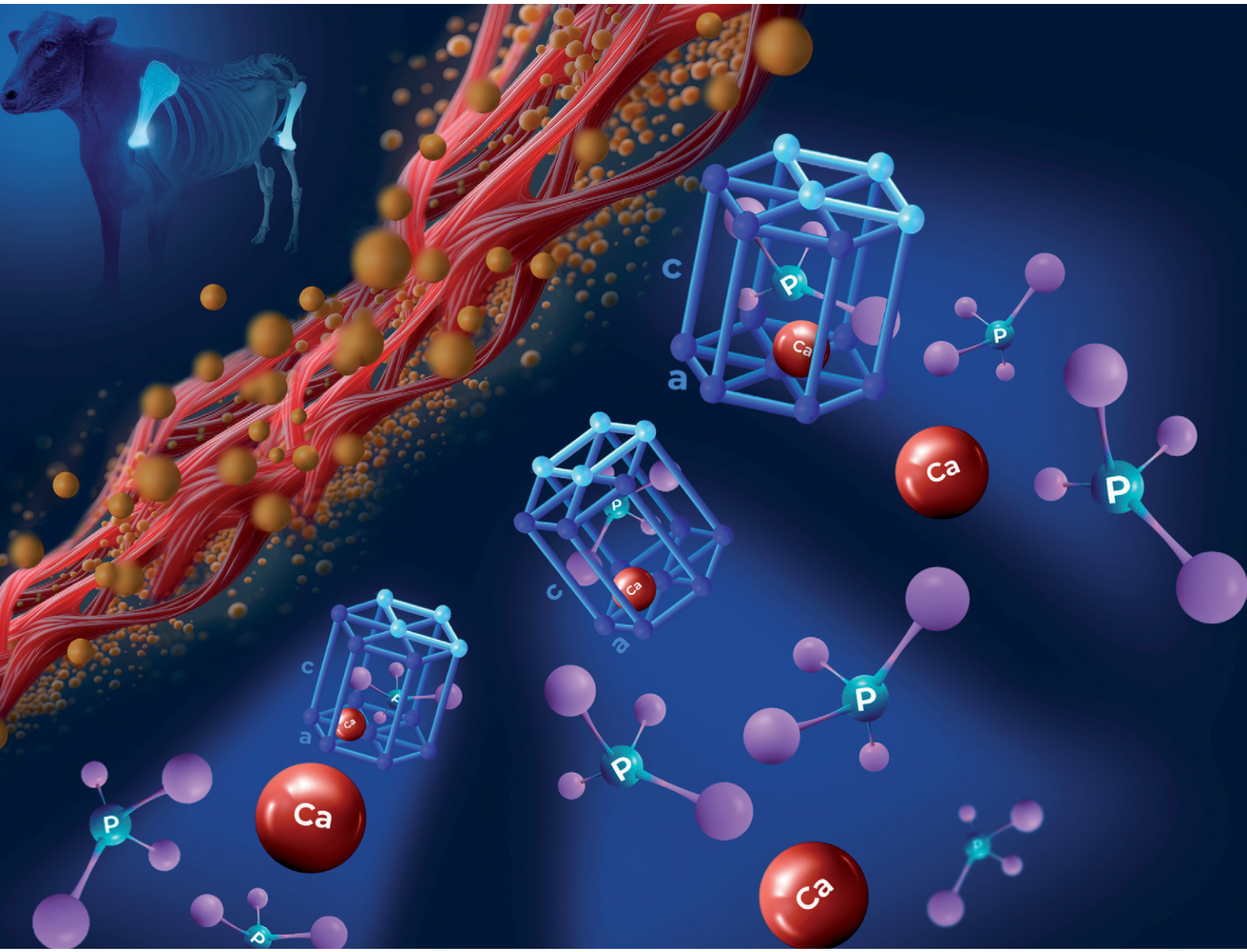

ISSN 2051-8153

ROYAL SOCIETY OF CHEMISTRY

PAPER
Marcelo E. Alves, Deb P. Jaisi *et al.*
Bone-derived hydroxyapatite: ultrastructure and tuning for controlled dissolution characteristics for a model nanofertilizer

Environmental Science Nano

ROYAL SOCIETY OF CHEMISTRY

PAPER

View Article Online
View Journal | View Issue

Check for updates

Cite this: *Environ. Sci.: Nano*, 2025, 12, 4850

Bone-derived hydroxyapatite: ultrastructure and tuning for controlled dissolution characteristics for a model nanofertilizer

Felipe H. dos Santos, [ab] Pavlo Ivanchenko, [a] Roger Borges, [c] Cauê R. de Oliveira, [c] Marcos Y. Kamogawa, [d] Marcelo E. Alves *[bd] and Deb P. Jaisi *[a]

Received 14th August 2025,
Accepted 24th September 2025

DOI: 10.1039/d5en00756a

rsc.li/es-nano

Calcium phosphate nanoparticles have been increasingly propounded as an efficient phosphorus (P) fertilizer in crop production. In this study, we used sustainable sourcing of calcium phosphates by recycling bovine bones and modifying the extracted hydroxyapatite using three approaches: calcination and mechano-activation, alkaline hydrolysis, and subcritical water extraction. Hydroxyapatites derived from these treatments were analyzed for ultrastructure, particle size distribution and crystal chemistry to interpret the dissolution characteristics under a flow-through nanofiltration system. While calcination was the most effective treatment for removing organic molecules—with only 0.22 wt% of total organic carbon and 0.03 wt% nitrogen remaining on hydroxyapatite—it led to the largest growth in crystallite size (113–139 nm) compared to hydroxyapatites treated through alkaline hydrolysis (45–93 nm) or subcritical water (33–78 nm). Surprisingly, the mechano-activated hydroxyapatite following the calcination exhibited a sustained and high P release profile, driven by the presence of ultrafine (10–35 nm) amorphous particles mixed with well-ordered and structurally defective apatitic structures. Hydroxyapatites recovered by alkaline hydrolysis and subcritical water treatments exhibited slow and steady P release profiles reflecting fewer structural and surface imperfections compared to mechano-activated hydroxyapatite. These findings demonstrate that processing-induced ultrastructural and compositional changes in bone-derived hydroxyapatite exert a major role in P-release characteristics. Consequently, these products could be tuned for both sufficiency and efficiency of P fertilization, thus generating sustainably sourced nano P fertilizer for crop production.

Environmental significance

Conventional phosphorus (P) fertilizers derived from limited geological reserves are excessively soluble and contribute to environmental issues such as eutrophication of water sources, algae blooms and hypoxia. Hydroxyapatite nanoparticles are a promising source for slow-P release, but are commonly synthesized from high-purity P sources. This study presents sustainable alternatives for sourcing hydroxyapatite from bovine bones, tuned for controlled P release through the processing parameters to address dual challenges in agriculture: sufficiency and efficiency. The structure–function relationships presented may be pivotal to the advancement of the new generation of P fertilizers.

Introduction

Phosphorus (P) is an essential element for all known life forms on Earth. For plants in particular, P is a macronutrient involved in key physiological processes such as photosynthesis and respiration. In field crops, P is absorbed from the soil solution, and the content of P removed from the soil with harvested biomass is typically replenished *via* the application of organic and mineral fertilizers. However, the finiteness of geological reserves mined to P fertilizer production,[1] combined with the rising P demand in biofuel crop production[2] or non-fertilizer applications such as battery and drug manufacturing,[3] has contributed to the spike in the value of P commodities. In the context of rising P fertilizer costs, the potential ramifications include decreased fertilizer application by farmers and a consequent decline in crop yields, which may ultimately undermine the global food security.[1]

One significant strategy to mitigate the strain on P reserves is the development of innovative fertilizers that

[a] *Interdisciplinary Science and Engineering Laboratory, University of Delaware, Newark, DE 19716, USA. E-mail: jaisi@udel.edu; Fax: +1 302 831 0605; Tel: +1 302 831 1376*
[b] *Department of Soil Science, Luiz de Queiroz College of Agriculture, University of São Paulo, Piracicaba, SP 13418-900, Brazil. E-mail: mealves.esalq@usp.br; Tel: +55 19 3429 4189*
[c] *Nanotechnology National Laboratory for Agriculture, Brazilian Agricultural Research Corporation, São Carlos, SP 13560 970, Brazil*
[d] *Department of Exact Sciences, Luiz de Queiroz College of Agriculture, University of São Paulo, Piracicaba, SP 13418-900, Brazil*

enhance P uptake by plants and attenuate P losses from soils.[4] Conventional P fertilizers, such as triple superphosphate, mono-ammonium phosphate and diammonium phosphate, are highly water-soluble, leading to their premature dissolution that is not synchronized with the P uptake kinetics by crops. In contrast, calcium phosphate (CaP) nanoparticles with tunable properties—such as synthetic hydroxyapatite,[5,6] modified hydroxyapatite,[7,8] or amorphous calcium phosphate (ACP)[9,10]—have been explored for application as slow-release P fertilizers. However, the synthesis of CaP typically relies on high-grade P sources such as phosphoric acid or monohydrogen phosphate salts, which primarily come from finite geological reserves.[11]

The recovery of P from sustainable sources, particularly from bones of animals raised and slaughtered for meat[12] offers a promising alternative to mitigate the pressure on geological reserves of P,[13] and, more importantly, enhances the circularity in the fertilizer sector. Historically, bones have been applied as fertilizer materials for centuries, albeit with low P use efficiency.[14] Conventional bone processing methods, including grinding, autoclaving, combustion, acidulation, or pyrolysis, often produce materials with subpar properties for fertilizers in terms of achieving high P recovery efficiency. In addition, these mentioned methods tend to overlook the bone structure assembly, which is essential for tuning materials for target applications. The highly hierarchical composite structure of mineralized collagen fibrils[15] has been known for over three centuries and has recently been better resolved through advancement of 3D imaging.[16] The bone mineral, also known as bioapatite, is a nano-sized CaP phase precipitated from animal body fluids[17] that if properly isolated from the organic fraction, has the potential to serve as a slow-release P fertilizer.[18]

Bioapatite constitutes approximately 55–60% of bone weight, far exceeding collagenous proteins found at 30%, water at 10–15%, and the small fraction of non-collagenous proteins and lipids.[17,19] Compared to stoichiometric hydroxyapatite, bioapatite is a calcium (Ca) and hydroxyl (OH^-) deficient structure ($P6_3/m$), and can contain up to 7 wt% of carbonate (CO_3^{2-}) and 3 wt% structural water.[20] In addition, bioapatite surfaces contain amorphous layers enriched with protonated phosphates such as HPO_4^{2-},[21] which contribute to their higher solubility compared to stoichiometric hydroxyapatite or fluorapatite.[22] The extraction of bioapatite for application as a P fertilizer could be a promising route to address dual challenges in agriculture: providing a secondary source of P and offering a slow-release mechanism for P fertilization. Nonetheless, the choice of processing method is crucial for the preparation of bioapatite as a slow-release fertilizer, as different methods can lead to significant variations in composition, crystallinity, and particle size distributions.[23]

Among bone processing methods, calcination is usually the standard method for recovering bioapatite, which leads to a notable increase in P concentration compared to raw bone. However, processing temperatures exceeding 700 °C may promote significant recrystallization of bioapatite.[25] To enhance the dissolution of calcinated apatite, the mechanical activation method is preferred over acidulation. This is because the conventional acidulation method generates phosphogypsum ($CaSO_4{\cdot}2H_2O$) as a by-product, which poses a disposal challenge for the P fertilizer industry.[26] Alternatively, hydrothermal treatment methods, such as alkaline hydrolysis, can be attractive due to lower operational costs compared to calcination and mechanical activation, while also offering higher selectivity for removing organic matter from bones.[23,27] Nevertheless, alkaline hydrolysis requires the use of strong alkaline reagents, a limitation that can be bypassed by employing treatments solely involving water. For example, near critical conditions—ranging from 100 to 374 °C and 100 kPa to 22.1 MPa—induce significant alteration in the physicochemical properties of water, most notably in the dielectric constant (ε). At 25 °C, water has an ε of 78.3, which drops to 27 at 250 °C above 100 kPa, similar to the dielectric constant of organic solvents such as methanol (ε = 33), or ethanol (ε = 25). Hence, the polarity of subcritical water enables effective extraction of organic matter from bones,[23] while preserving bioapatite in comparison to calcination and alkaline hydrolysis methods.

The objectives of this research are to investigate the effect of three different bone treatment methods on the composition, structure, and size of nanometric apatite, and to understand how these characteristics affect the P dissolution kinetics at a pH typical of root exudates. To the best of our knowledge, the application of apatites extracted through alkaline hydrolysis or subcritical water as fertilizers has not been previously evaluated.

Materials and methods

Reagents and terminology

The following analytical grade reagents were utilized for processing, extraction and analysis: potassium hydroxide (KOH, ≥ 99.0% pure, Synth), sodium hydroxide (NaOH, ≥ 99.0% pure, Synth), sodium citrate dihydrate ($Na_3C_6H_5O_7{\cdot}2H_2O$, ≥ 99%, Ricca Chem), anhydrous citric acid (> 99%, Acros), nitric acid (HNO_3, 70%, Thermo Fisher) and hydrochloric acid (HCl, 37%, Thermo Fisher).

The terms bone mineral, bone apatite, biological apatite (bioapatite), hydroxyapatite, and carbonated hydroxyapatite are commonly used in the scientific literature as synonyms to describe the mineral fraction of bone. The bioapatite nomenclature reflects the biological mineralization of bone minerals, in contrast to their geological or synthetic crystallization. Nonetheless, apatite is a generic term used for a group of 15 minerals, which is more strictly used to refer to a subgroup of three minerals: fluorapatite, chlorapatite, and hydroxyapatite.[24] An amorphous surface layer and a highly disordered apatitic core, both differing from stoichiometric hydroxyapatite, make it difficult to apply more specific, appropriate terminology to bone minerals, particularly given

that the properties of non-processed minerals differ substantially from those of the processed materials. Therefore, we have used the generic term bioapatite to refer to the non-processed CaP phase present in bone, whereas hydroxyapatite (HA) is hereafter used collectively to refer to processed and altered CaP, despite the limitations.

Collection and pre-treatment of bones

Bones—specifically femurs and scapulae—from 3-year-old bovines were collected from a butcher shop (Fig. S1). The bones were cut into pieces measuring 5 (±2) cm and repeatedly washed in boiling deionized water to remove residual meat and bone marrow. Subsequently, the bone pieces were autoclaved at 120 °C and 98 kPa for 1 h to both sterilize them and reduce their mechanical resistance to fragmentation. Thereafter, the pieces were oven-dried at 65 °C for 48 h and fragmented using a micropulverizer mill (R-TE-350, Tecnai), then sieved to obtain particles ≤ 2 mm. The resulting bone powder, prepared exclusively through the pre-treatment described, is hereafter referred to as 'HAut'. This preparation was preferred over the use of commercial bone meal as a source of bioapatite due to variations in raw materials and processing conditions among different suppliers.

Recovery of hydroxyapatite from bones

Calcination of bones was employed to remove organic matter and to recover purified HA. The calcination of HAut was conducted in an electric muffle furnace with a heating rate of 15 °C min^{-1} until reaching 600 °C, which was maintained for 2 h. The procedure was conducted with the muffle lid open to facilitate gas exchanges, which resulted in temperature variation of ±20 °C. The HA recovered after calcination is henceforth referred to as 'HAc'. Nominally, 25 g of HAc were mechano-activated for 1 h at 380 rpm using an orbital mill (model CT-242, Servitech). The activation was performed using alumina balls with a ball-to-powder mass ratio of 10 : 1. The material recovered after calcination and mechano-activation is referred to as 'HAcm'. Alternatively, hydrothermal treatments of bones were performed using deionized water or potassium hydroxide (KOH).[28] Briefly, 2 g of HAut was mixed with 60 mL of either deionized water (<0.05 μS cm^{-1}) or 0.5 mol L^{-1} KOH solution in Teflon containers. Teflon containers were then placed in a steel reactor under constant magnetic stirring, maintaining temperature (200 °C) and pressure (≥30 bar), for 5 h following a reported method.[23] The solids were then separated from the supernatant by centrifugation at 8000 rpm, and the resulting pellets were subsequently freeze-dried. The HA isolated by the alkaline treatment is designated as "HAk" while the HA recovered using water under subcritical conditions is referred to as "HAw".

Chemical composition of hydroxyapatites

To monitor the changes in HA composition after treatments, all samples were subjected to acid digestion for elemental analysis, each performed in triplicates. The HA samples and a bone meal standard reference material (NIST1486) were digested separately with a 3 : 1 mixture of HNO_3 and HCl using EPA method 3051A in a microwave furnace (CEM, NC). The extracts were analyzed for Al, B, Ca, Cu, Fe, K, Mg, Mn, Na, P, S, and Zn by inductively coupled plasma optical emission spectroscopy (ICP-OES) using a Thermo 7600 ICAP (Thermo Elemental, WI).

Total carbon (TC) and nitrogen (N) contents were determined in duplicate using the Pregl-Dumas combustion method with an Elementar VarioMax CN Analyzer (Elementar Americas, NJ). Total organic carbon (TOC) was measured after removing inorganic carbon with 1 mol L^{-1} HCl.[27] The total inorganic carbon (TIC) content was calculated as the difference between TC and TOC. Additionally, thermogravimetric (TGA) and differential scanning calorimetry (DSC) analyses were simultaneously conducted with an SDT Q600 analyzer (TA Instruments, DE) to estimate the CO_3^{2-} content and the mass loss events during heating. For thermal analysis, the furnace was programmed to heat at a rate of 10 °C min^{-1} up to 160 °C, followed by a 30 min isothermal step to eliminate adsorbed water, and then continued heating at a ramp of 10 °C min^{-1} until reaching 1000 °C. All thermal analyses were performed under a synthetic air atmosphere at a flow rate of 50 mL min^{-1}.

Fourier transform infrared spectroscopy (FTIR)

FTIR was used to identify the residual organic molecules after various treatments. Spectra were collected by using a Nicolet 380 FTIR spectrometer (Thermo, NJ) equipped with an attenuated total reflectance (ATR) accessory with a single-reflection diamond crystal. The HA samples were firmly pressed using a dynamometric clamp to ensure consistent contact with the crystal surface. The spectral range selected was from 400 to 4000 cm^{-1} with 128 scans performed to ensure an optimal signal-to-noise ratio. The resulting spectra were baseline-corrected and normalized to the asymmetric stretching mode ν_3 P–O around 1065 cm^{-1} using OPUS software (v 8.2, Bruker).

Raman spectroscopy

Raman was employed to distinguish among various phosphate species in HAs subjected to different treatments. Since Raman signals arise from the polarizability of ions, which are presented as relative positions and shapes of the Raman bands, it provides complementary information to FTIR. Raman spectra were acquired using a diode laser operating with a fixed wavelength of 786 nm and an output power of 50 mW (Kaiser, Endress, and Hauser, IN). Each spectrum was recorded with an exposure time of 0.5 s and accumulated 64 spectra per measurement point. The collected spectra were also baseline-corrected but normalized to the symmetric stretching mode ν_1 P–O around 960 cm^{-1} using OPUS software.

Synchrotron-based X-ray diffraction (sXRD)

sXRD was used to investigate the mineral phases and crystallite sizes of different HA. Diffraction patterns were collected at the Paineira beamline at the LNLS[29] with a heavy-duty 3-circle diffractometer (Newport Co., CA). The diffractometer was operated in transmission mode using Debye–Scherrer geometry. Images were recorded using a PiMega 450D fast detector array (πTec Co., BRA) which utilized Medipix3RX ASIC sensors arranged in an arc configuration. This setup provided an angular coverage of 2–109° and 0.07° resolution for full width at half maximum (FWHM), and rapid detection capabilities (30 s per sample). Increment steps of 2θ = 0.007° resulted in 15 285 scans per HA sample analyzed.

The HAs were loaded into Kapton capillaries (Ø = 1.37 mm), sealed at both ends with epoxy putty, and then mounted in magnetic spinner-type sample holders (Fig. S2). Data acquisition was performed in high-throughput mode with automated spinner exchange. An X-ray beam energy of 15.99 keV, equivalent to a wavelength of 0.7749 Å was used in data collection. The data were converted to CuKα wavelength (1.5406 Å) using the following formula to enable comparison with standard powder diffraction files (PDF): $\lambda_1 \sin(\theta)_2 = \lambda_2 \sin(\theta)_1$, where λ_1 = 0.7749 Å (conversion of 15.99 keV to wavelength), λ_2 = 1.54 Å (CuKα wavelength), and $\sin(\theta_1)$ and $\sin(\theta_2)$ are the sines of the respective diffraction angles. Diffraction data were then processed using the software Match! (Crystal Impact, Bonn). The FWHM values were extracted after full-profile fitting employing the goodness-of-fit (GoF) parameter to optimize the peak profile matching. The Scherrer equation was applied to calculate coherent domain sizes (D) as follows: $D = \frac{K\lambda}{\beta \cos(\theta)}$, where K is a dimensionless shape factor (0.9), λ is the wavelength of CuKα radiation (1.54 Å), and β is the FWHM (radian). Separate domain size calculations were made for the D_{002} and D_{310} planes of the crystal lattice,[30] instead of calculating average values. Furthermore, 10 peaks from each diffractogram were chosen to calculate D, which were then plotted using kernel density estimation (KDE) to visualize their probability distribution.

High-resolution transmission electron microscopy (HR-TEM)

HRTEM was employed to investigate particle size and morphology. Micrographs were acquired with a Talos F200C (Thermo Fischer, OR) at an acceleration potential of 200 kV, with a beam size of 0.9 nm and an analytical probe current of 1.58 nA. The HA powders were dispersed in ethanol using an ultrasonic water bath and then three droplets were deposited on a 300-mesh carbon–copper grid. To minimize potential artifacts due to electron beam bombardment, beam alignment was conducted in areas of non-interest and micrographs were collected with minimal exposure time.

The interplanar distance (d-spacing) of the HA particles was calculated from analysing HRTEM micrographs using ImageJ software (National Institutes of Health, USA), in which pixel counting in the software was calibrated according to the known distances in nm. Image areas with no visible superposition of particles or lattice planes were selected for fast Fourier transform (FFT) analysis. Selected reflections were filtered, and inverse FFT was applied to convert back into the spatial domain, isolating the lattice fringes. The d-spacing was then calculated using the average distance between 10 or more visible fringes. The TEM-based lattice data were compared to those derived from d-spacing in the X-ray diffraction data.

Scanning electron microscopy (SEM) energy-dispersive X-ray spectroscopy (EDS)

SEM-EDS was employed to differentiate HAcm particles from mill fragments. Three-dimensional imaging and analysis of HA were performed with an AURIGA 60 Crossbeam (Zeiss, GER) at an accelerating voltage of 15 kV and a beam size of 1–5 nm. The HA samples were deposited on a carbon stub and sputter-coated with Pd/Au for 30 s to ensure the electron conductivity of the surfaces. EDS spectra were collected from specific particle agglomerates to identify the constituent elements.

Dissolution of hydroxyapatites

A customized flow-through nanofiltration system was employed to investigate the difference in P dissolution kinetics of HAs derived from bones. The setup and extractant have been thoroughly described previously.[6,7,10] In brief, the setup features a continuous flow of the extractant through the HA dispersed powder, while minimizing the formation of the Nernst diffusion layer. The 0.01 mol L^{-1} citric acid buffer solution used as the extractant was prepared by dissolving 1.57 g of sodium citrate in 800 mL of deionized water, followed by the addition of 0.89 g of citric acid. The buffer pH was adjusted to 4.80 using 0.1 M NaOH. Then, deionized water was added to achieve a final volume of 1000 mL.

Triplicates of 50 mg HA powder were first dispersed in 1 mL of ethanol using 1.5 mL vials sealed at the edges with a sealing film, agitated on a vortex mixer, and then kept in a sonication water bath for approximately 150 min. Thereafter, each HA sample was homogeneously deposited onto a 10 kDa membrane disc (equivalent to a pore size of 5–6 nm). A second 10 kDa membrane filter was placed above the sample to prevent direct contact of the inflowing solution with the HA and to maintain the uniformity of the deposited layer. This assembly was then placed inside a 10 mL ultra-filtration cell (Fig. S3), and 2 mL of citrate buffer was added on top. In the sequence, an effective residual pressure of 50 psi was applied to the macro-dialysis cell, ensuring a flow rate of 50 μL s^{-1} of the extractant through the membrane. Eluted solutions (extracts) from the HA powder were collected every 5 s in separate vials over 80 s, yielding approximately 250 μL of extract per vial. The concentration of dissolved P in each eluate was determined using the phosphomolybdate blue

method at a wavelength of 881 nm (ref. 31) using a Cary 5000 UV-vis spectrophotometer (Agilent Technologies, CA).

Results and discussion

Chemical composition of hydroxyapatites

The elemental analyses of HA recovered from five different treatments (Fig. 1) showed remarkable variations in composition. A comparison of TOC and N contents shows that thermal treatments, such as calcination or calcination followed by mechano-activation, effectively removed most of the organic content from HAs (Table 1). Alkaline hydrolysis was nearly as effective as calcination in removing TOC and N. In contrast, the TOC content in HAw was around 16 times higher than that in HAc, while the difference in N content between two materials was considerably smaller. Compared to HAut, HAw exhibited a TOC/N ratio of approximately 20 while HAut had a TOC/N ratio around 4. This suggests that the subcritical water extraction may have been equally effective to thermal and alkaline treatments in removing proteins, but less effective in removing other biomolecules devoid of N, such as lipids.

The small amounts of TC and TOC detected in HAc in elemental analyses are consistent with the findings from TGA analysis. Note that TGA was primarily employed for estimating the carbonate content and thus indirectly assessing the organic C content (Fig. 2A). The least mass lost observed under oxidizing conditions at the temperature range of 250–600 °C occurred in HAc, with progressively higher mass losses recorded for HAcm, HAk, HAw, and HAut (Fig. 2A; Table S1). The first derivative of TGA in the range of 200–1000 °C revealed distinct regions of mass loss events related to the collagen and non-collageneous protein degradation, which starts at 327 °C and goes until around 450 °C. This interpretation is reinforced by the exothermic peaks at 338 °C and 445 °C in HAut (Fig. 2C) and by the observation of CO_2, N_2O, and NH_3 released in this temperature range in a previous study on bovine bone calcination.[25] The loss of structural water known to occur from 250–550 °C could not be spotted as in pristine HA[20] due to the presence of organic matter, while the loss of CO_3^{2-} in the 600–900 °C range appear overlapping the dehydroxylation and transformation of HA to β-tricalcium phosphate occurring from 700–1000 °C. Notably, both the mass loss events related to organic molecules and those associated with mineral transformations occurred at lower temperatures for HAut compared to HAw. Although HAut has a higher organic content than HAw, its molecular composition is likely different, as indicated by the previously discussed C/N ratio. Moreover, autoclaving of HAut probably denatured and fragmented proteins, decreasing their thermal stability, while in HAw the residual organic compounds may have become more condensed and associated with the HA.

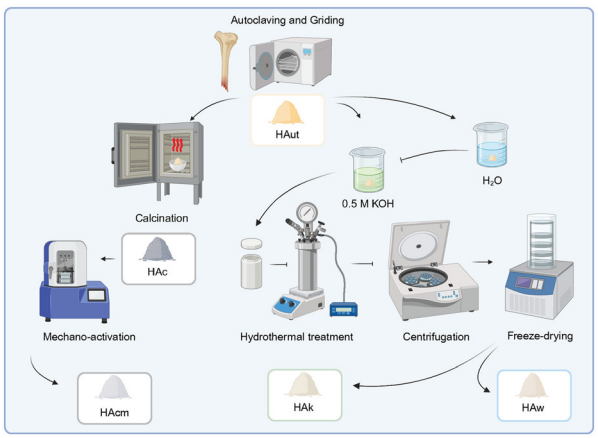

Fig. 1 Flowchart illustrating bone treatments and corresponding hydroxyapatite (HA) products: autoclaving (HAut), calcination (HAc), mechano-activation (HAcm), alkaline hydrolysis (HAk), and subcritical water extraction (HAw). The illustration was created using Biorender®.

Table 1 Carbon and nitrogen contents in hydroxyapatites extracted from bones in different treatments

Treatment	TC (%)	TOC (%)	N (%)
HAut	12.58 ± 0.01	11.59 ± 0.1	3.07 ± 0.03
HAc	0.37 ± 0.01	0.22 ± 0.04	0.03 ± 0.01
HAcm	0.56 ± 0.05	0.32 ± 0.01	0.04 ± 0.01
HAk	1.19 ± 0.07	0.53 ± 0.02	0.02 ± 0.01
HAw	5.45 ± 0.39	3.79 ± 0.11	0.19 ± 0.01

The organic residues in HA were qualitatively assessed using FTIR. The spectral range of 1650–1300 cm^{-1} in the FTIR spectra, which typically exhibits the ν_3CO_3 vibrational mode in HA, was overlapped by amide I (1650–1680 cm^{-1}) and amide II (1540–1550 cm^{-1}) bands in HAut (Fig. 3). The high intensity of HAut bands in the 1650–1300 cm^{-1} region relative to other treatments confirms the higher content of collagen and organic carbon in this material compared to other HA samples. In contrast, the intensities of amide I and II bands were significantly diminished in HAk and completely disappeared in HAc.

Notably, the intensities of amide bands, characterized predominantly by the C=O stretching band for amide I, and N–H bending for amide II, as well as C–H stretching bands (around 3000 cm^{-1}), revealed a higher intensity in HAw compared to both HAc and HAk. This observation is coherent with the results derived from TOC and TGA analysis. Interestingly, the C–H bands, which are of low intensity in HAc, disappear completely in the HAcm, likely due to transient temperatures reaching as high as 400–500 °C in localized microregions during ball collisions,[32] which may have contributed to the further volatilization of organic molecules.

In contrast to the TOC content, the highest content of TIC was found in HAw (1.67 wt%), followed by progressively lower contents in HAut (0.99 wt%), HAk (0.67 wt%), HAcm (0.24 wt%), and HAc (0.15 wt%). The higher TIC content in HAw than that in HAut indicates the incorporation of CO_3^{2-} during the subcritical water extraction process. Similarly, the CO_3^{2-} incorporation may have also occurred during the

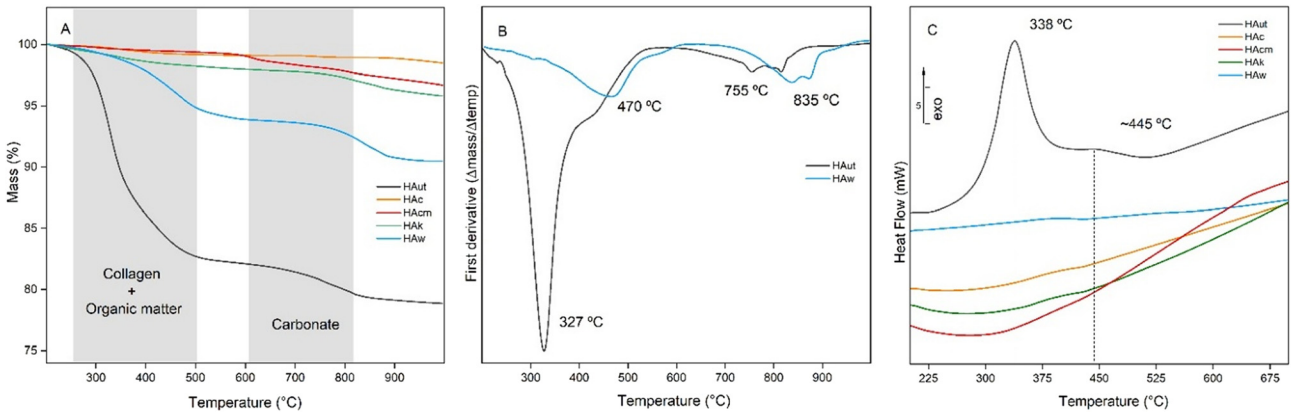

Fig. 2 A) Thermogravimetric analyses (TGA) of hydroxyapatites over the temperature range of 200–1000 °C. B) Derivative thermogravimetry (DTG) of TGA curves highlighting HAut, HAc, and HAcm treatments over the 200–1000 °C range, and C) differential scanning calorimetry (DSC) over the 200–700 °C range.

mechanochemical activation of HAc, as indicated by the higher TIC content in HAcm compared to HAc (Table S1). The higher CO_3^{2-} content in the HA structure correlates with the smaller crystal size and a lower degree of crystallinity,[33] which are evidenced in HAw and HAut materials (see the hydroxyapatite structure).

The TGA results corroborated the estimated TIC values calculated from elemental analysis. However, it is noteworthy that the content of CO_3^{2-} obtained from TGA was universally higher than the corresponding TIC estimations (Table S1). This discrepancy can be attributed to the intrinsic limitation inherent to the TGA methodology, wherein multiple overlapping mass loss events occur within a narrow or the same thermal range. Moreover, it is important to note that TIC and TGA results reflect calculated inorganic carbon values, facilitating the assessment of relative content among various HAs but should not be misconstrued as direct measurements. Nevertheless, the inorganic carbon estimations are significant to demonstrate, along with the crystallite size (see the hydroxyapatite structure section), that the most efficient treatments for removing TOC and N were those that imparted the more substantial modifications to HA properties.

A positive correlation was observed between the efficiency of organic removal during treatment and P content in the resultant HA (Table 2). Surprisingly, HAc was 1.5% richer in P than the HAcm, despite both materials being derived from HAut. This deviation might be partially attributed to the structural incorporation of CO_3^{2-}, as evidenced from TIC and TGA results, as well as the erosion of mill balls, which led to a higher Fe and Al content in HAcm compared to HAc (Table S1). The higher P content observed in HAk than that in HAw cannot be attributed to experimental artifacts but rather reflects the efficiency of alkaline hydrolysis in organic matter removal, as evidenced by a 3.6% difference in TOC between the two materials (Table 1) and a 5.4% difference in mass loss in the TGA results (Table S2). Overall, the average P content in potential innovative slow-release nanofertilizers (HAcm, HAk, HAw) was 16%, which lies between commercial acidulated P fertilizers such as single superphosphate (7–9% P) and triple superphosphate (20% P), and lower than NP fertilizers like monoammonium phosphate (23% P) and diammonium phosphate (20% P).

The trace element content of bioapatite varied among treatments. For instance, the K^+ content in HAcm was minimal and comparable to KOH treatment, suggesting that the alkaline treatment did not significantly facilitate the incorporation of K^+ into the HAk structure. A trace amount of $Zn^{2+}$was found in all treatments, which is presumed to be partial substitution of Ca II sites in seven-fold coordination. The Ca II site—with a Ca^{2+} ionic radius of 1.07 Å—is more exposed and accessible to accommodate ions with ionic radii between 0.9 and 1.3 Å. This range includes smaller ions such as Zn^{2+} and Mg^{2+} and larger ions including Pb^{2+}, Sr^{2+}, and Na^+. The minor difference in the ionic radii between Ca^{2+} and Na^+ (1.13 Å, in seven-fold coordination),[34] combined with Na^+ higher electronegativity

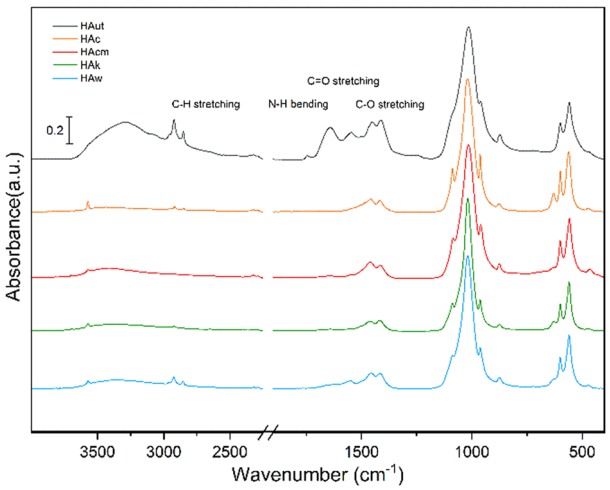

Fig. 3 FTIR-ATR spectra in the 4000–400 cm^{-1} mid-infrared region of hydroxyapatites recovered from bovine bones.

Table 2 Chemical composition of hydroxyapatites isolated from bones obtained after acid dissolution and ICP-OES quantification (n.d. = not detected; <300 mg kg^{-1} for K). See Table S1 for the trace element composition

Treatment	Ca	P	Mg	Na	K	CCa/P ratio
	g kg^{-1}					
HAut	263.51 ± 2.06	121.20 ± 0.19	4.49 ± 0.06	5.82 ± 0.03	n.d.	1.68
HAc	374.04 ± 0.82	171.33 ± 0.17	6.54 ± 0.01	8.62 ± 0.02	0.35 ± 0.03	1.69
HAcm	349.80 ± 0.47	156.29 ± 0.16	6.72 ± 0.01	8.26 ± 0.04	0.94 ± 0.03	1.73
HAk	366.62 ± 0.07	165.38 ± 0.48	6.58 ± 0.03	3.01 ± 0.02	0.92 ± 0.01	1.71
HAw	345.61 ± 2.12	157.94 ± 0.32	5.48 ± 0.04	3.47 ± 0.02	n.d.	1.69

and abundance in body fluids relative to K^+ (1.46 Å), accounts for the observed high content of Na^+ in the HA structure.

The Ca/P molar ratios of HA varied in the range of 1.68–1.73, which is slightly higher than the stoichiometric HA (1.67). It is well recognized that the biological apatites do not adhere to a fixed composition; typically, the Ca/P ratios are lower than the stoichiometric HA. These ratios can range from 1.3 to 1.5 in the ACP found in young bones, and from 1.5 to 1.67 in more crystalline and mineralized mature bones.[35] The measured Ca/P ratio of 1.68 in HAut is consistent with the mature bones of a 3-year-old cow used as the source of bioapatite. However, it remains uncertain whether the slightly elevated Ca/P ratio in HAut is attributed to ionic substitutions, vacancies at PO_4^{3-} sites, or P depletion during processing. If P depletion is the primary cause, it appears that autoclaving, calcination, and subcritical water extraction lead to less P loss compared to alkaline hydrolysis. The higher Ca/P ratio observed in HAcm, in contrast to HAc, is consistent with the thermogravimetric results, suggesting the incorporation of inorganic C during mechanochemical activation, a finding which is further supported by the results from Raman spectroscopy (Fig. 4).

The Raman spectra of HA revealed notable peaks corresponding to the symmetric stretching mode of the phosphate group (ν_1) around 960 cm^{-1}. This peak demonstrates a pronounced sensitivity to variations in the chemical environment within the HA structure. In addition, Raman peaks at around 925 cm^{-1} are indicative of protonated phosphate species (HPO_4^{2-} or $H_2PO_4^-$, hereafter collectively referred to as HPO_4^{2-}), in a P–O–H^+ bond configuration.[17] The presence of H^+ in HA nanoparticles is a critical factor for enhancing the dissolution, as highlighted in a previous study.[7]

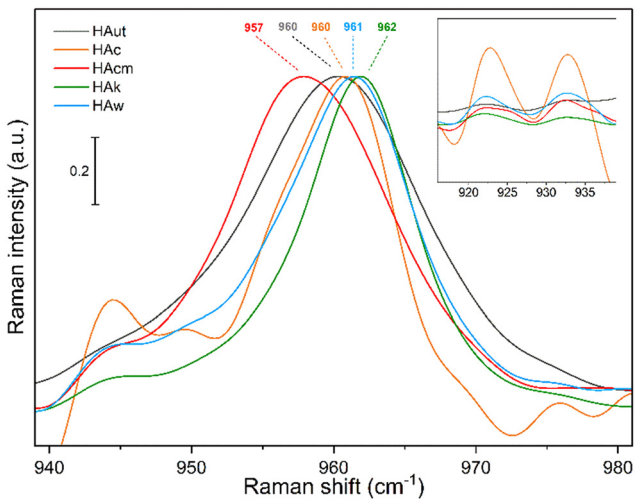

Fig. 4 Raman spectra in the 940–980 cm^{-1} region showing phosphate (PO_4^{3-}) symmetric stretching vibration (ν_1) and the 915–940 cm^{-1} region characteristic of acid phosphates.

A comparative analysis among different HAs revealed that HAcm displays a lower Raman shift with a maximum intensity at 957 cm^{-1}. In contrast, the other HAs exhibited Raman shifts: HAut at 960.2 cm^{-1}, HAc at 960.8 cm^{-1}, HAw at 961 cm^{-1}, and HAk at 962 cm^{-1}. The relatively lower Raman shift observed for HAcm indicates a weaker P–O bond, which may be attributed to the structural disorder, since its proton content was relatively lower than HAc, HAw, and HAut. The apparent discrepancy between the lowest Raman shift of HAcm at 957 cm^{-1} and the median intensity around 925 cm^{-1} —correlated to the HPO_4^{2-} content[17]—can be explained by the mechanical activation of HAc. This activation potentially facilitates reactions with the adsorbed molecules such as CO_2, leading to their incorporation into the structure and causing subsequent disorder (see morphology section). This hypothesis is supported by the elemental quantification data revealing that HAcm has the second lowest P content, which cannot be fully explained by mill fragments (Table S2). Conversely, a high HPO_4^{2-} content of HAc, shown by the Raman band of around 925 cm^{-1}, may stem from the loss of structural water and the initial stages of dehydroxylation, which can generate vacancies and free H^+ ions available for the reaction with PO_4^{3-}.[36] In stark contrast, the smallest HPO_4^{2-} content of HAk is consistent with the effect of alkaline treatment, during which potential dissolution and recrystallization of HAk may have consumed H^+ ions previously bound to PO_4 groups. In summary, these findings exhibit the intricate relationship between the structural characteristics of HAs, its H^+ content, and structural integrity under different treatment conditions.

Hydroxyapatite structure

The well-defined crystalline structure of HAs following treatments facilitated the acquisition of diffraction patterns with a high signal-to-noise ratio (Fig. 5). Notably,

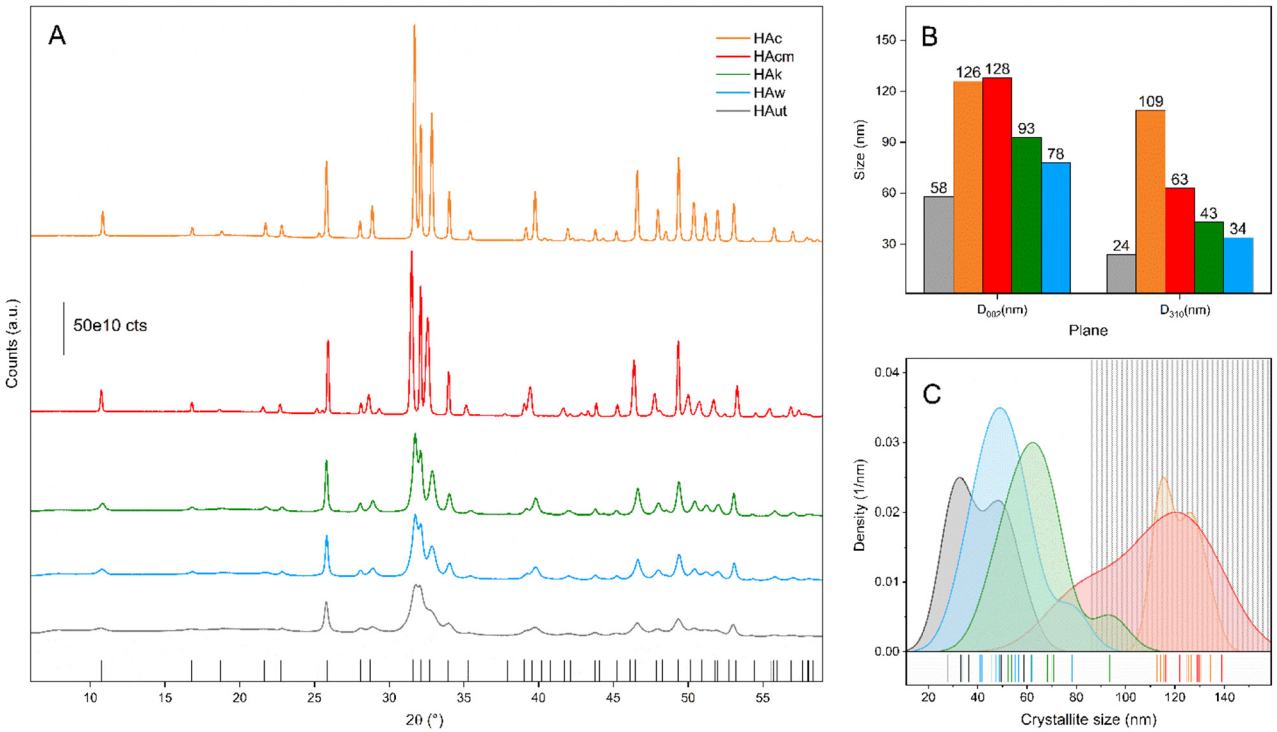

Fig. 5 A) sXRD patterns of HA recovered from bovine bones. Vertical black lines below the diffraction patterns represent peak positions of carbonated-hydroxyapatite JCPDS card 969003552. B) Crystallite size dimensions along the [002] and [310] directions. C) Crystallite size distribution plotted employing kernel density. The colored lines below the curves represent individual crystallite size, calculated using the Scherrer equation. The color coding in legend A corresponds to the color used in B and C.

no phase changes were detected across various bone processing methods used, with hydroxyapatite (96-900-3552) identified as the sole mineral, similarly to previous reports.[21,37] The HAcm treatment revealed additional peaks at 2θ = 25.4°, 29.3°, and 43.1°, attributed to aluminium oxide (96-230-0449), correlating with the elevated aluminium content observed in comparison to the HAc treatment (Table S2). No calcium oxide (CaO) was observed, as expected, since CaO formation typically occurs when treating bone above 700 °C.[38]

While the absence of phase changes was confirmed, the increased photon counts for the (211), (112), and (300) diffraction peaks, in conjunction with larger crystallite dimensions along the [002] and [310] directions across all treatments compared to HAut (Fig. 5B), suggest the occurrence of recrystallization. Distinct impacts were noted for each treatment; for instance, the crystallite size of HAc in the [310] direction was more than fourfold larger compared to HAut, whereas the difference when comparing HAk and HAut was considerably less pronounced. Intriguingly, mechano-activation of HAc resulted in a reduction of crystallite size by approximately 50% along the [310] direction, with no notable change in the [002] direction (Fig. 5B). The subcritical water extraction caused the least impact on the bioapatite structure, as evidenced by the crystallite dimensions of HAw and HAut, which is consistent with previous results (see the hydroxyapatite composition section). Alkaline hydrolysis exhibited an intermediate effect on bioapatite crystallinity, between subcritical water and calcination followed by mechanochemical activation. Overall, the crystallite dimensions and respective impact of different treatments on bioapatite are as follows: HAut < HAw < HAk < HAc and HAcm.

The influence of the bone as a whole cannot be overlooked when evaluating the outcomes of treatments on HAs. Bone is a composite material with significant variability in structure and composition, largely dictated by its functional role.[16] Such heterogeneity is observed when comparing distinct bones in an animal (*e.g.*, long bones *vs.* flat bones), distinct anatomical regions of a single bone (*e.g.*, cortical *vs.* trabecular tissue), bones at different developmental stages (*e.g.*, juvenile *vs.* mature), and bones from different species (*e.g.*, bovine *vs.* chicken femur).[38,39] At a molecular level, variations among bones can be detected in the content and identity of both collagenous and non-collagenous proteins.[39] In turn, the bioapatite content in bone may exhibit variations in composition, degree of crystallinity, and position relative to collagen fibrils.[13] Previous studies have explored the collagen/bioapatite ratio as a proxy for differences in mechanical properties among bones.[40] This is particularly relevant to the processing of bones to recover HAs, given that the organic matrix serves as a thermal barrier and inhibits recrystallization during treatments. For instance, heating the cortical portion of avian tibia from 100 °C to 800 °C in 100 °C increments did not result in significant recrystallization of bioapatite integrated

within collagen fibrils until the complete removal of the organic matrix, which occurred around 600 °C.[41] In contrast, bioapatite embedded in non-collagenous proteins such as proteoglycans present in the medullary portion of tibia revealed evidences of recrystallization at a significantly lower temperature, around 400 °C.[41] Calcination of the cortical portion of bovine femur (from 100 to 1000 °C) resulted in no significant recrystallization until surpassing the 600–700 °C range,[25] and no secondary phase transformation, such as the conversion of HA to β-tricalcium phosphate, was reported before reaching 1100 °C in cortical bovine femur subjected to calcination.[42] Notably, a ratio of 53 : 47 wt% of HA : β-tricalcium phosphate was observed following the treatment of fish bone at 850 °C for 1 h[43] underscoring the influence of the collagen/bioapatite content on thermal processing outcomes across different bones. Although calcination of HAut (femur and scapulae) resulted in a more pronounced increase in crystallite size compared to hydrothermal treatments, the observed effect could have been magnified with a less mineralized bone or higher processing temperatures.

The influence of bone composition on hydrothermal processing is noteworthy, yet a direct comparison with existing literature data present challenges due to the limited range of processing conditions evaluated, particularly compared to the calcination method.[25,42] An exception to this observation was found in a recent study,[28] which assessed the effects of varying NaOH or KOH concentrations (0.5 and 2 mol L^{-1}) and treatment time (2 to 10 days) on the HA recovered from the cortical portion of bovine bones. Their findings indicated that the prolonged treatment time and higher concentration of NaOH promoted crystal growth, thereby lending support to the dissolution–reprecipitation mechanistic interpretation.

For the assessment of crystallite size distribution in anisotropic HA crystals in this study, 10 peaks exhibiting high signal-to-noise ratios were selected from the diffraction data. This estimation, visualized through kernel density distribution, facilitated the categorization of HAs into two groups: those recovered *via* hydrothermal treatments *versus* those processed using thermal treatment (Fig. 5C). Not surprisingly, the bimodal distribution of the HAut exhibited the smallest size range, varying from 27 to 59 nm. In comparison, crystallite size distributions of HAw and HAk exhibited slightly larger dimensions than HAut, with centroids at 45 nm for HAw and 60 nm for HAk (Fig. 5C). For HAc, the distribution was centered around 120 nm, which is threefold higher relative to HAk and HAw. Similarly, HAcm exhibited a broad size distribution, likely attributed to the combination of the sintering process during calcination (see the morphology section) and preferential cleavage along the *a* or *b* axes during mechanochemical activation.

Raman and HRTEM analyses indicated a significant presence of amorphous material in HAcm, highlighting the

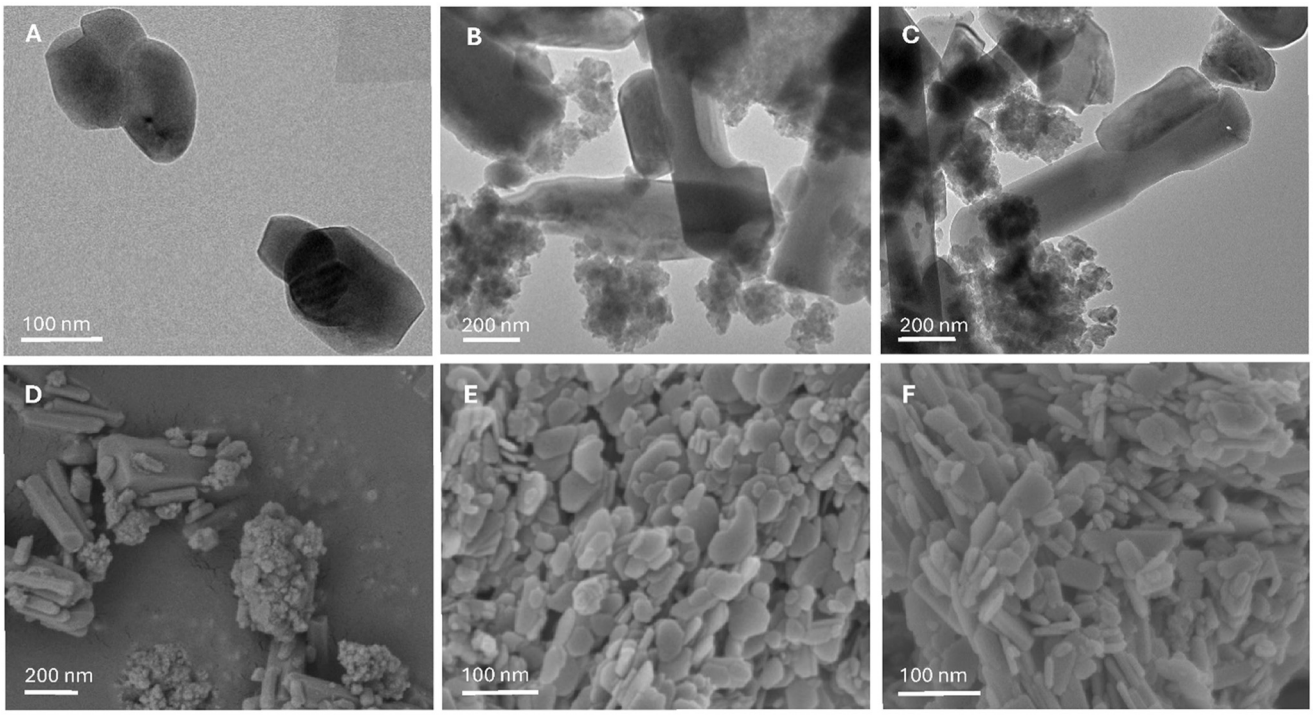

Fig. 6 Electron micrographs of dispersed hydroxyapatite particles isolated from bovine bones following different treatments. A) High-resolution TEM micrograph of HAc (magnification of 120 k), highlighting merged grain boundaries; B and C) high-resolution TEM micrograph of HAcm (magnification of 120 k) highlighting fractal-like agglomerates of ultrafine amorphous particles and broken or strained nanorods; D) SEM micrograph of HAcm (magnification of 40 k) displaying the morphological and size heterogeneity; E and F) SEM micrographs of HAk and HAw (magnification of 100 k), revealing nano-platelets less heterogeneous in morphology and size compared to HAcm.

limitation of the crystallite size calculation from sXRD patterns for estimating particle size. As such, the overall constitution of HAcm encompass a broader spectrum of particles in terms of size and crystallinity.

Particle size and morphology of hydroxyapatites

HRTEM and SEM micrographs provided valuable insights into the potential mechanisms involved during HAut treatments. The micrographs of HAc (Fig. 6A) and HAcm (Fig. 6C) display platelets characterized by merged boundaries, which are characteristic features of the sintering process. Notably, the images from HAcm (Fig. 6B and C) reveal several agglomerates composed of amorphous particles with dimensions ranging from 10 to 35 nm, as corroborated by Raman spectroscopy. However, these entities were not detected in the XRD analysis and thus were excluded from the crystallite size distribution. Additionally, HRTEM micrographs of HAcm (Fig. S4) exhibited platelets measuring 75 to 234 nm with irregularly rounded edges, as well as rod-shaped particles varying from 211 to 2553 nm in length and 79 to 311 nm in the minor axis. The rod-shaped particles observed in the HAcm micrographs demonstrated fractures and strained edges because of the mechano-activation process, features that were absent in HAc.

To ascertain the composition of amorphous particles observed in HAcm, the SEM-EDS technique was utilized. The results affirmed that these particles were predominantly composed of Ca, O, and P (Fig. S5), consistent with the composition of calcium phosphates. The notable carbon content detected in the EDS analysis which originated from the carbon stub did not interfere with the detection of Ca and P, nor did it compromise the confirmed absence of Al in the amorphous particles. Summing these findings, it is reasonable to conclude that the platelets and rods originated from HAc, while the fractal-like aggregates of amorphous particles emerged during the mechano-activation process. The abundance of ultrafine amorphous materials associated with the distinct larger rods and platelets likely played a critical role in enhancing the dissolution of HAcm (see the hydroxyapatite dissolution section).

HRTEM micrographs of HAk and HAw revealed a more uniform distribution of particles in terms of size and shape (Fig. 6E and F). HAk consisted of platelets measuring 20 to 50 nm and rods ranging from 29 to 107 nm in length, with widths of 12 to 40 nm (n = 50). In contrast, HAw displayed platelets of 18 to 38 nm and rods measuring 26 to 73 nm in length and a width of 12 to 40 nm (n = 50). Given that the solvent was the only variable between the alkaline hydrolysis and subcritical water extraction, the observed difference in the particle size distributions further confirms that the greater extent of recrystallization occurred in HAk compared to HAw. The fringes visible in the HRTEM micrographs of HAk exhibited d-spacings consistent with the (111) and (110) of HA, as identified through sXRD (Fig. S4). Similarly, the fringes observed in HAw were compatible with the (111), while HAcm showed fringes corresponding to the d-spacing (210). The HRTEM micrographs of HAut displayed agglomerated rods embedded in the organic matrix measuring 32 to 74 nm in length and 19 to 51 nm in width. Additionally, an extra dimension measuring 4 to 7 nm, consistent with the platelet thickness of bioapatite in mature bovine bone,[44] was noted in HAut. However, TEM does not allow for distinguishing this dimension from the width of the rods (Fig. S5).

Hydroxyapatite dissolution characteristics

Previous studies showed that nano-HA dissolution in a conventional batch system is limited to approximately 30% due to proton depletion from organic acids,[45] directing subsequent advancements toward flow-through systems and buffered solutions containing the major carboxylates present in the rhizosphere of crops, such as citrate, oxalate, and acetate.[7,8,11] Here, the P release rates in the citrate buffer varied markedly among HAcm, HAk, and HAw materials, highlighting differences in their composition and the corresponding role of dissolution. The dissolution of HAut and HAc was omitted because the primary focus was on the nanometric HAs, which are promising P fertilizers.[9,46] Analysis of dissolution data shows that HAcm released a cumulative total of 418 μg of P (8.37 μg mg^{-1} of HAcm), which accounts for 5.36 wt% of its total P content. In contrast, HAk released a notably smaller mass of P (92 μg, 1.86 μg mg^{-1} of HAk), which corresponds to only 1.12% of its total P. Interestingly, HAw showed the lowest P release both in terms of mass (1.38 μg mg^{-1} of HAw) and volume of the extractant, totalling 68 μg of P, representing a mere 0.87% of its total P.

While thermodynamic solubility remains unchanged between nano-HA and micro-HA, dissolution kinetics is significantly accelerated in the nanomaterial, which was expected to lead to higher dissolution rates of HAw and HAk compared to HAcm. However, the influence of structural

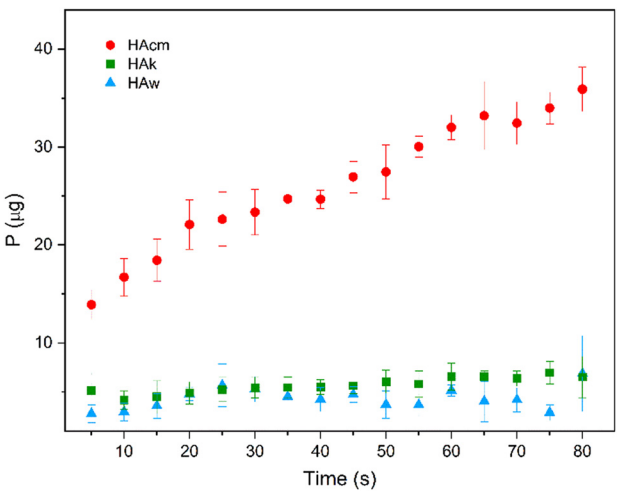

Fig. 7 Kinetics of P released over dissolution experiments from HAcm, HAk, and HAw. Error bars represent standard deviation (n = 3).

defects and compositional differences in HAcm appears to override the effect of particle size, thereby enhancing P release from HAcm compared to other nano-HA (Fig. 7). Specifically, the distinct dissolution pattern of HAcm may be attributed to its higher H^+ content compared to HAk, as evidenced by the relative intensity of bands around 925 cm^{-1} in Raman spectroscopy, and to the heterogeneity in particle size and degree of crystallinity revealed from HRTEM and sXRD analyses, respectively.

The initial rapid dissolution phase in the HAcm release curve, followed by a 20–40 s plateau, likely results from the dissolution of ultrafine amorphous particles and structurally flawed surfaces of rods and platelets (Fig. S4). This stage precedes micrometric particle dissolution and is followed by a second plateau (65–75 s), indicating more crystalline regions beneath the surface that temporarily delay further dissolution. The dissolution mechanism likely involves the formation of kink sites[47] with mechanical shocks in HAcm creating reactive sites for H^+, thus enhancing initial dissolution. As the reaction progresses into less imperfect regions, additional activation energy may be needed for further dissolution. Variability in the HAw dissolution pattern is attributed to residual organic molecules (Table 1), which interferes with surface reactivity and hinders reproducibility. Despite its lower dissolution rate, HAk showed the least variable P release pattern, highlighting consistency for potential process engineering replicability. The lower and slower P release from HAk and HAw is likely due to fewer structural and surface imperfections, resulting in fewer reactive sites. Interestingly, the P mass released from both HAk and HAw remained around 5 μg over time, despite decreasing HA mass.

A blend of amorphous, strained, and crystalline particles exhibiting an irregular step-terrace surface structure was observed in HAcm (Fig. 8), probably enhancing dissolution.

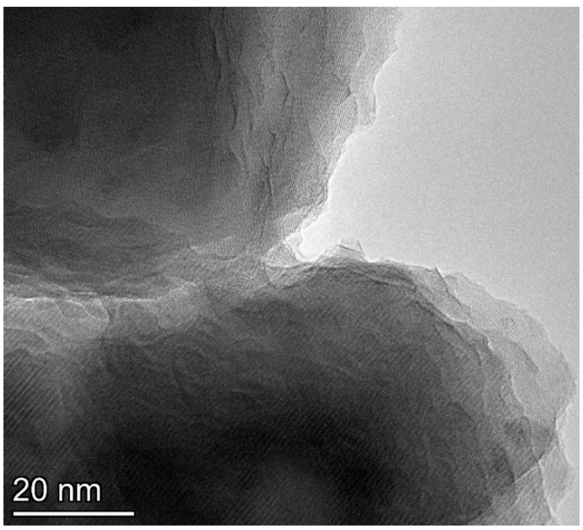

Fig. 8 High-resolution transmission electron micrograph depicting the formation of the step-terrace structure on HAcm surfaces during dissolution (magnification of 510 k).

Amorphous particles present in HAcm may exhibit similarities with amorphous calcium phosphate (ACP) in terms of structural disorder[48] and enhanced solubility.[49] EDS results of amorphous particle agglomerates in HAcm provided semi-quantitative estimates (Fig. S5), with a Ca/P ratio of 2.09, which is within ACP ranges (1.0–2.2).[49]

Interestingly, a contrasting trend in P release from HA and citrate-stabilized ACP has been documented.[10] This contrast may indicate that P release from HAcm, consisting of ultrafine amorphized particles and HA, may produce a sigmoidal pattern over extended dissolution periods. If so, this product may be an ideal model for slow-release fertilizers.[50] Given that bone is a natural source and both calcination and mechano-activation are physical treatments, HAcm may even serve as a nanofertilizer for providing supplant P in organic farming systems.

Potential application of biogenic hydroxyapatite as a P fertilizer

Enhancing plant productivity through nano-based fertilizers has emerged as a prominent topic in plant and soil sciences,[51] with HA standing out as the most studied nanomaterial in P nutrition. The nano-HA charge was highlighted as a significant property for particle transport and P release in soils.[8,52,53] For comparison, the HAcm ζ-potential in DLS measurements was −30.5 mV (n = 7). Nanometric HAs with ζ-potentials of −13.8 mV, −1.4 mV, and +22.1 mV were synthetized and applied as a source of P to sunflower (*Helianthus annuus*)[8] which exhibited the greatest increase in shoot and root dry biomass when grown in an Ultisol (pH 4.7) treated with −13.8 mV HA. However, it is unclear whether increased yields were related to the higher mobility or to enhanced dissolution of the negatively charged nanorods promoted by its citrate functionalization: formation of citrate complexes with Ca enhances the dissolution of HA[47] and influences particle morphology through preferential adsorption onto the *a* and *b* crystal axes, yielding rod-shaped particles—elongated along the *c*-axis—with different surface environments.[54] Nonetheless, the higher mobility presented by HA particles with −13.8 mV ζ-potential in column experiments[8] suggests a promising way to enrich weathered soils in Ca and P at a depth below 20 cm. The stimulated root growth in the subsurface zone of soils due to Ca and P presence is broadly associated with increased drought tolerance by plants,[55] a significant advantage in times of climate change that is hardly addressed when using conventional P fertilizers. HAcm application in this potential advancement was envisioned by results observed in tomato (*Solanum lycopersicum*) grown in a clayey soil—44% clay and pH 6.8—fertilized with biogenic nano-HA—prepared from bovine bones calcined at 750 °C for 3 hours followed by ball milling—which exhibited superior or comparable performance in root-related parameters, including fresh and dry root biomass and root length, compared to treatments with an unspecified calcium phosphate salt.[56] Future studies are warranted to further investigate the influence of nano-HA

charge and morphology on transport within soil matrices, particularly when avoiding the powdered combination with soils that can create micrometric aggregates of surface reactive nano-HA, which may obscure results and interpretation of experimental outcomes, oftentimes considered unclear.[57]

The interactions between HA nanorods obtained by mechano-activation of microcrystalline HA and P-deficient barley roots were evaluated in a hydroponic system.[46] The HA nanorods exhibited a ζ-potential ranging between −25 and −30 mV due to citrate and foreign ion incorporation and successfully provided P to plants, restoring physiological functions associated with the element in less than 48 hours. Interestingly, it was found that P contained in nanocrystalline HA was dissolved prior to uptake at the root cap region, while in mature epidermal and cortical cells, the particles were able to penetrate the apoplastic region before being fully dissolved.[46] Unfortunately, the effects of mechanical treatment on the HA structure and dissolution were not evaluated, hindering comparison with HAcm.

Conclusions

The complementary techniques used to characterize the HA in this study aided in interpreting the dissolution characteristics and developing structure–function relationships. Here, a key factor affecting the dissolution of HAcm was the presence of a significant portion of amorphous particles (10–35 nm range), which contributed to an initial rapid P release, followed by a gradual and sustained release from the dissolution of crystalline particles. The smaller crystallite sizes observed in HAw, relative to HAk, HAcm, and HAc, imply that subcritical water extraction had the least impact on structural integrity. This may be due to the incomplete removal of organic molecules, which could act as buffering agents and influence dissolution rates, which were fully explored in this study. Future studies should focus on optimizing extraction parameters—time, temperature, and pressure—to enhance organic carbon removal and understand their effects on HAw properties. It is noted that the advancements in subcritical water extraction are warranted because of its environmental sustainability and purity of HAw.

The P release profile of HAcm is expected to correlate with the P uptake kinetics of many crops, suggesting its potential as an effective slow-release fertilizer. If so, this approach may enhance P recovery by plants compared to conventional P fertilizers. It is important to highlight that the transition from bench-scale research to greenhouse and field applications presents an opportunity for integrated assessments of P use efficiency and economic viability, including the energy balance associated with calcination and milling processes. Optimizing processing parameters to minimize costs should be a key factor for developing scalable and sustainable fertilizer production. Such efforts, tied with environmental benefits of bone waste valorization and P recycling, could offer economic value while reducing dependence on geogenic P sources.

Author contributions

This study was conceived by F. H. S., M. E. A., and D. P. J. The data collection was carried out by F. H. S., P. I., and R. B. Data checking was carried out by F. H. S., P. I., R. B., M. E. A., and D. P. J. Data discussion and interpretation were performed by F. H. S., P. I., R. B., M. E. A., M. Y. K., C. R. O., and D. P. J. The first manuscript draft was written by F. H. S. and edited by P. I., R. B., M. E. A., and D. P. J.

Conflicts of interest

The authors declare no conflict of interest.

Data availability

Supplementary information: includes six figures and two tables. The figures include: bones at different processing stages (Fig. S1); the experimental setup and sample orientation for XRD experiments (Fig. S2); flow-through macro-dialysis system set up for dissolution (Fig. S3); SEM and HRTEM micrographs of HAs (Fig. S4); SEM micrographs and EDS spectra of ultrafine particles in HAcm (Fig. S5); and a scatter plot with trend lines showing the relationship between cumulative volume (μL) and cumulative P mass (μg) for three different HAs (Fig. S6). Tables include the trace element content in HAs recovered from bovine bones (Table S1) and organic carbon from mass loss at the 250–600 °C range in TGA and inorganic carbon from 600–900 °C (Table S2). See DOI: **https://doi.org/10.1039/D5EN00756A**.

All data are included in the text and supporting information (SI).

Acknowledgements

The authors acknowledge the support from the Paineira beamline team at the Brazilian Synchrotron Light National Laboratory for XRD data collection, with special thanks to Fernando da Silva and Cristiane Rodella. Additional thanks are due to Gerald Poirier and his team in the Advanced Material Characterization Laboratory of the University of Delaware for their assistance in the spectroscopic and microscopic data collection. The authors acknowledge financial support from the São Paulo Research Foundation (FAPESP) through a Ph.D. fellowship [2022/11235-8, FHS and MEA] and a research internship abroad [2023/09890-0, FHS and MEA]. Additional support was provided by the U.S. Department of Agriculture, National Institute of Food and Agriculture (USDA-NIFA) through research grants [2023-67021-39521 and 2023-69016-39062, DPJ].

References

1 D. Cordell, J. O. Drangert and S. White, The story of phosphorus: Global food security and food for thought, *Global Environmental Change-Human and Policy Dimensions*, 2009, **19**(2), 292–305, DOI: **10.1016/j.gloenvcha.2008.10.009**.

2 L. Hein and R. Leemans, The impact of first-generation biofuels on the depletion of the global phosphorus reserve, *Ambio*, 2012, **41**(4), 341–349, DOI: **10.1007/s13280-012-0253-x**.

3 B. M. Spears, W. J. Brownlie, D. Cordell, L. Hermann and J. M. Mogollón, Concerns about global phosphorus demand for lithium-iron-phosphate batteries in the light electric vehicle sector, *Commun. Mater.*, 2022, **3**(1), 14, DOI: **10.1038/s43246-022-00236-4**.

4 P. Y. Wang, P. Das, L. Wang, J. Y. Zhou, C. Y. Deng, I. Vera-Reyes, C. O. Dimkpa, J. C. White and Y. Wang, Prospects of nano phosphorus fertilizers (NPFs) in plant-based agriculture: effects and mechanisms, *J. Nanopart. Res.*, 2025, **27**(3), 60, DOI: **10.1007/s11051-025-06261-x**.

5 R. Liu and R. Lal, Synthetic apatite nanoparticles as a phosphorus fertilizer for soybean (Glycine max), *Sci. Rep.*, 2014, **4**, 5686, DOI: **10.1038/srep05686**.

6 Y. Sakhno, C. X. Ma, J. Borgatta, Y. Jin, J. C. White and D. P. Jaisi, Role of cation substitution and synthesis condition in a calcium phosphate-based novel nanofertilizer on lettuce (*Lactuca sativa*) yield, *ACS Sustainable Chem. Eng.*, 2022, **10**(47), 15414–15422, DOI: **10.1021/acssuschemeng.2c04451**.

7 Y. Sakhno, I. Miletto, G. Paul and D. P. Jaisi, A novel route to enhance the dissolution of apatite: Structural incorporation of hydrogen phosphate, *Nanoimpact*, 2022, **28**, 100422–100432, DOI: **10.1016/j.impact.2022.100422**.

8 L. Xiong, P. Wang, M. N. Hunter and P. M. Kopittke, Bioavailability and movement of hydroxyapatite nanoparticles (HA-NPs) applied as a phosphorus fertiliser in soils, *Environ. Sci.: Nano*, 2018, **5**(12), 2888–2898, DOI: **10.1039/c8en00751a**.

9 Y. Sakhno, L. Degli Esposti, A. Adamiano, J. Borgatta, J. C. White, M. Iafisco and D. P. Jaisi, Citrate-stabilized amorphous calcium phosphate nanoparticles doped with micronutrients as a highly efficient nanofertilizer for environmental sustainability, *ACS Agric. Sci. Technol.*, 2023, **3**(10), 845–854.

10 Y. Sakhno, S. Vaidya, M. Nikolenko, J. C. White, M. Iafisco and D. P. Jaisi, Comparative analysis of crystalline hydroxyapatite and amorphous calcium phosphate for dissolution and plant nutrition, *J. Nanopart. Res.*, 2025, **27**, 151, DOI: **10.1007/s11051-025-06338-7**.

11 K. Schrödter, G. Bettermann, T. Staffel, F. Wahl, T. Klein and T. Hofmann, Phosphoric acid and phosphates, in *Ullmann's encyclopedia of industrial chemistry*, ed. B. Elvers, Wiley-VCH Verlag GmbH & Co., 2012.

12 A. Hart, K. Ebiundu, E. Peretomode, H. Onyeaka, O. F. Nwabor and K. Obileke, Value-added materials recovered from waste bone biomass: technologies and applications, *RSC Adv.*, 2022, **12**(34), 22302–22330, DOI: **10.1039/d2ra03557j**.

13 L. Pilotto, M. Y. A. Zuluaga, F. Scalera, C. Piccirillo, L. Marchiol, M. Civilini, Y. Pii, S. Cesco and G. Fellet, Sustainable crop fertilization by combining biogenic nano-hydroxyapatite and P solubilizing bacteria: Observations on barley, *Plant Nano Biol.*, 2024, **9**, 100091, DOI: **10.1016/j.plana.2024.100091**.

14 K. D. Jacob, Predecessor of Superphosphate, in *Superphosphate: Its History, Chemistry, and Manufacture*, ed. USDA, US, Department of Agriculture and Tennessee Valley Authority, 1964, pp. 8–18.

15 H. Sheldon and R. A. Robinson, Electron microscope studies of crystal-collagen relationships in bone .4. The occurrence of crystals within collagen fibrils, *Journal of Biophysics and Biochemistry*, 1957, **3**(6), 1011–1016, DOI: **10.1083/jcb.3.6.1011**.

16 D. J. Buss, R. Kröger, M. D. McKee and N. Reznikov, Hierarchical organization of bone in three dimensions: A twist of twists, *J. Struct. Biol.: X*, 2022, **6**, 100057, DOI: **10.1016/j.yjsbx.2021.100057**.

17 B. Wopenka and J. D. Pasteris, A mineralogical perspective on the apatite in bone, *Mater. Sci. Eng. C*, 2005, **25**(2), 131–143, DOI: **10.1016/j.msec.2005.01.008**.

18 F. Carella, M. Seck, L. D. Esposti, H. Diadiou, A. Maienza, S. Baronti, P. Vignaroli, F. P. Vaccari, M. Iafisco and A. Adamiano, Thermal conversion of fish bones into fertilizers and biostimulants for plant growth-A low tech valorization process for the development of circular economy in least developed countries, *J. Environ. Chem. Eng.*, 2021, **9**(1), 104815–104826, DOI: **10.1016/j.jece.2020.104815**.

19 M. J. Glimcher, Bone: Nature of the calcium phosphate crystals and cellular, structural, and physical chemical mechanisms in their formation, *Rev. Mineral. Geochem.*, 2006, **64**, 223–282, DOI: **10.2138/rmg.2006.64.8**.

20 J. D. Pasteris, C. H. Yoder and B. Wopenka, Molecular water in nominally unhydrated carbonated hydroxylapatite: The key to a better understanding of bone mineral, *Am. Mineral.*, 2014, **99**, 16–27.

21 S. Von Euw, Y. Wang, G. Laurent, C. Drouet, F. Babonneau, N. Nassif and T. Azaïs, Bone mineral: new insights into its chemical composition, *Sci. Rep.*, 2019, **9**, 8456, DOI: **10.1038/s41598-019-44620-6**.

22 S. V. Dorozhkin, Calcium orthophosphates in nature: Biology and medicine, *Materials*, 2009, **2**(2), 399–498, DOI: **10.3390/ma2020399**.

23 N. A. M. Barakat, K. A. Khalil, F. A. Sheikh, A. M. Omran, B. Gaihre, S. M. Khil and H. Y. Kim, Physiochemical characterizations of hydroxyapatite extracted from bovine bones by three different methods: Extraction of biologically desirable HAp, *Mater. Sci. Eng. C*, 2008, **28**(8), 1381–1387, DOI: **10.1016/j.msec.2008.03.003**.

24 J. M. Hughes and J. F. Rakovan, Structurally robust, chemically diverse: Apatite and Apatite supergroup minerals, *Elements*, 2015, **11**(3), 165–170, DOI: **10.2113/gselements.11.3.165**.

25 M. Greiner, A. Rodríguez-Navarro, M. F. Heinig, K. Mayer, B. Kocsis, A. Göhring, A. Toncala, G. Grupe and W. W. Schmahl,

Bone incineration: An experimental study on mineral structure, colour and crystalline state, *J. Archaeol. Sci. Rep.*, 2019, **25**, 507–518, DOI: **10.1016/j.jasrep.2019.05.009**.

26 L. F. O. Silva, M. L. S. Oliveira, T. J. Crissien, M. Santosh, J. Bolivar, L. Y. Shao, G. L. Dotto, J. Gasparotto and M. Schindler, A review on the environmental impact of phosphogypsum and potential health impacts through the release of nanoparticles, *Chemosphere*, 2022, **286**(Part 1), 131513–131527, DOI: **10.1016/j.chemosphere.2021.131513**.

27 J. I. Hedges and J. H. Stern, Carbon and Nitrogen Determinations of Carbonate-Containing Solids, *Limnol. Oceanogr.*, 1984, **29**(3), 657–663, DOI: **10.4319/lo.1984.29.3.0657**.

28 J. Brzezinska-Miecznik, P. Jelen, K. Haberko, W. Mozgawa and M. Sitarz, The effect of NaOH and KOH treatment on the behavior of CO and OH groups in natural origin hydroxyapatite, *Ceram. Int.*, 2017, **43**(15), 12540–12545, DOI: **10.1016/j.ceramint.2017.06.127**.

29 F. R. Estrada, D. H. Barrett, A. I. Ferreira, J. C. Mauricio, H. Rigamonti, B. C. Meyer, H. C. N. Tolentino, H. Westfahl and C. B. Rodella, PAINEIRA beamline at Sirius: an automated facility for polycrystalline XRD characterization, *J. Phys.: Conf. Ser.*, 2022, **2380**, 012033.

30 J. M. Delgado-López, R. Frison, A. Cervellino, J. Gómez-Morales, A. Guagliardi and N. Masciocchi, Crystal size, morphology, and growth mechanism in bio-inspired apatite nanocrystals, *Adv. Funct. Mater.*, 2014, **24**(8), 1090–1099, DOI: **10.1002/adfm.201302075**.

31 J. Murphy and J. P. Riley, A modified single solution method for the determination of phosphate in natural water, *Anal. Chim. Acta*, 1962, **27**, 31–36.

32 I. H. Tsai, C. W. Huang, C. F. Chang and E. W. G. Diau, Solvent-free ball milling synthesis of water-stable tin-based pseudohalide perovskites for photocatalytic CO reduction, *Small*, 2025, **21**(3), 2409023, DOI: **10.1002/smll.202409023**.

33 A. C. Deymier, A. K. Nair, B. Depalle, Z. Qin, K. Arcot, C. Drouet, C. H. Yoder, M. J. Buehler, S. Thomopoulos and G. M. Genin, Protein-free formation of bone-like apatite: New insights into the key role of carbonation, *Biomaterials*, 2017, **127**, 75–88, DOI: **10.1016/j.biomaterials.2017.02.029**.

34 R. D. Shannon, Revised effective ionic radii and systematic studies of interatomic distances in halides and chalcogenides, *Acta Crystallogr., Sect. A*, 1976, **32**, 751–767, DOI: **10.1107/S0567739476001551**.

35 L. T. Kuhn, M. D. Grynpas, C. C. Rey, Y. Wu, J. L. Ackerman and M. J. Glimcher, A comparison of the physical and chemical differences between cancellous and cortical bovine bone mineral at two ages, *Calcif. Tissue Int.*, 2008, **83**(2), 146–154, DOI: **10.1007/s00223-008-9164-z**.

36 M. P. Sternlieb, J. D. Pasteris, B. R. Williams, K. A. Krol and C. H. Yoder, The structure and solubility of carbonated hydroxyl and chloro lead apatites, *Polyhedron*, 2010, **29**(11), 2364–2372, DOI: **10.1016/j.poly.2010.05.001**.

37 J. R. Zhou, T. K. Yao, D. M. Cao, J. Lian and F. Y. Lu, In-situ TEM study of radiation-induced amorphization and recrystallization of hydroxyapatite, *J. Nucl. Mater.*, 2018, **512**, 307–313, DOI: **10.1016/j.jnucmat.2018.10.018**.

38 K. D. Rogers and P. Daniels, An X-ray diffraction study of the effects of heat treatment on bone mineral microstructure, *Biomaterials*, 2002, **23**(12), 2577–2585, DOI: **10.1016/S0142-9612(01)00395-7**.

39 A. L. Boskey and P. G. Robey, The composition of bone, in Primer on the metabolic bone diseases and disorders of mineral metabolism, ed. B. E. Al, 2019, pp. 84–92.

40 K. D. Rogers and P. Zioupos, The bone tissue of the rostrum of a whale: a mammalian biomineral demonstrating extreme texture, *J. Mater. Sci. Lett.*, 1999, **18**(8), 651–654, DOI: **10.1023/A:1006615422214**.

41 A. B. R. Navarro, S. Madero, M. Greiner, P. A. Rodríguez-Jimenez, W. W. Schmahl and C. Jiménez-López, Effect of heating on avian (cortical and medullary) bone chemistry, mineralogy and structural organization, *Cryst. Growth Des.*, 2023, **23**(11), 7841–7852, DOI: **10.1021/acs.cgd.3c00648**.

42 C. Y. Ooi, M. Hamdi and S. Ramesh, Properties of bhydroxyapatite produced by annealing of bovine bone, *Ceram. Int.*, 2007, **33**(7), 1171–1177, DOI: **10.1016/j.ceramint.2006.04.001**.

43 S. Righi, E. Prato, G. Magnani, V. Lama, F. Biandolino, I. Parlapiano, F. Carella, M. Iafisco and A. Adamiano, Calcium phosphates from fish bones in sunscreen: An LCA and toxicity study of an emerging material for circular economy, *Sci. Total Environ.*, 2023, **862**, 160751, DOI: **10.1016/j.scitotenv.2022.160751**.

44 S. J. Eppell, W. D. Tong, J. L. Katz, L. Kuhn and M. J. Glimcher, Shape and size of isolated bone mineralites measured using atomic force microscopy, *J. Orthop. Res.*, 2001, **19**(6), 1027–1034, DOI: **10.1016/S0736-0266(01)00034-1**.

45 D. Wang, Y. Xie, D. P. Jaisi and Y. Jin, Effects of low-molecular-weight organic acids on the dissolution of hydroxyapatite nanoparticles, *Environ. Sci.: Nano*, 2016, **3**, 768–779, DOI: **10.1039/c6en00085a**.

46 A. E. Szameitat, A. Sharma, F. Minutello, A. Pinna, M. Er-Rafik, T. H. Hansen, D. P. Persson, B. Andersen and S. Husted, Unravelling the interactions between nano-hydroxyapatite and the roots of phosphorus deficient barley plants, *Environ. Sci.: Nano*, 2021, **8**(2), 444–459, DOI: **10.1039/d0en00974a**.

47 S. V. Dorozhkin, Dissolution mechanism of calcium apatites in acids: A review of literature, *World J. Methodol.*, 2012, **2**(1), 1–17, DOI: **10.5662/wjm.v2.i1.1**.

48 E. D. Eanes, Amorphous calcium phosphate, in *Monographs in oral science: Octacalcium phosphate*, ed. L. C. Chow and E. D. Eanes, 2001, pp. 130–147.

49 S. V. Dorozhkin, Synthetic amorphous calcium phosphates (ACPs): preparation, structure, properties, and biomedical applications, *Biomater. Sci.*, 2021, **9**(23), 7748–7798, DOI: **10.1039/d1bm01239h**.

50 M. E. Trenkel, *Slow- and controlled-release and stabilized fertilizers: An option for enhancing nutrient efficiency in agriculture*, IFA, Paris, France, 2010.

51 E. Santos, G. S. Montanha, M. H. F. Gomes, N. M. Duran, C. G. Corrêa, S. L. Z. Romeu, A. E. S. Pereira, J. L. Oliveira, E. Almeida and A. Pérez-de-Luque, *et al.*, Are nanomaterials leading to more efficient agriculture? Outputs from 2009 to 2022 research metadata analysis, *Environ. Sci.: Nano*, 2022, **9**(10), 3711–3724, DOI: **10.1039/d1en01078f**.

52 D. J. Wang, Y. Jin and D. P. Jaisi, Effect of size-selective retention on the cotransport of hydroxyapatite and goethite nanoparticles in saturated porous media, *Environ. Sci. Technol.*, 2015, **49**(14), 8461–8470, DOI: **10.1021/acs.est.5b01210**.

53 L. Xiong, P. Wang and P. M. Kopittke, Tailoring hydroxyapatite nanoparticles to increase their efficiency as phosphorus fertilisers in soils, *Geoderma*, 2018, **323**, 116–125, DOI: **10.1016/j.geoderma.2018.03.002**.

54 P. Ivanchenko, J. M. Delgado-López, M. Iafisco, J. Gómez-Morales, A. Tampieri, G. Martra and Y. Sakhno, On the surface effects of citrates on nano-apatites: evidence of a decreased hydrophilicity, *Sci. Rep.*, 2017, **7**, 8901, DOI: **10.1038/s41598-017-09376-x**.

55 M. M. Aslam, J. K. Karanja, I. C. Dodd, M. Waseem and W. F. Xu, Rhizosheath: An adaptive root trait to improve plant tolerance to phosphorus and water deficits?, *Plant, Cell Environ.*, 2022, **45**(10), 2861–2874, DOI: **10.1111/pce.14395**.

56 A. Baroutkoob, M. Haghighi and M. A. Hajabbasi, Amending clayey and sandy soils with nano - bio phosphorous for regulating tomato growth, biochemical, and physiological characteristics, *Sci. Rep.*, 2024, **14**(1), 24975, DOI: **10.1038/s41598-024-76389-8**.

57 P. M. Kopittke, E. Lombi, P. Wang, J. K. Schjoerring and S. Husted, Nanomaterials as fertilizers for improving plant mineral nutrition and environmental outcomes, *Environ. Sci.: Nano*, 2019, **6**(12), 3513–3524, DOI: **10.1039/c9en00971j**.